J. Fluid Mech. (1996), *vol.* 319, *pp.* 281–303

Three-dimensional transition of natural-convection flows

By R. A. W. M. HENKES[1] AND P. LE QUÉRÉ[2]

[1]Delft University of Technology, J. M. Burgers Centre for Fluid Mechanics, Faculty of Aerospace Engineering, PO Box 5058, 2600 GB Delft, The Netherlands

[2]LIMSI/CNRS, PO Box 133, F-91403 Orsay Cédex, France

(Received 14 February 1995 and in revised form 20 March 1996)

The stability with respect to two- and three-dimensional perturbations of natural-convection flow of air in a square enclosure with differentially heated vertical walls and periodic boundary conditions in the lateral direction has been investigated. The horizontal walls are either conducting or adiabatic. The solution is numerically approximated by Chebyshev–Fourier expansions. In contrast to the assumption made in earlier studies, three-dimensional perturbations turn out to be less stable than two-dimensional perturbations, giving a lower critical Rayleigh number in the three-dimensional case for the onset of transition to turbulence. Both the line-symmetric and line-skew-symmetric three-dimensional perturbations are found to be unstable. The most unstable wavelengths in the lateral direction typically are of the same size as the enclosure. In the nonlinear solution new symmetry breaking occurs, giving either a steady or an oscillating final state. The three-dimensional structures in the nonlinear saturated solution consist of counter-rotating longitudinal convection rolls along the horizontal walls. The energy balance shows that the three-dimensional instabilities have a combined thermal and hydrodynamic nature. Besides the stability calculations, two- and three-dimensional direct numerical simulations of the weakly turbulent flow were performed for the square conducting enclosure at the Rayleigh number 10^8. In the two-dimensional case, the time-dependent temperature shows different dominant frequencies in the horizontal boundary layers, vertical boundary layers and core region, respectively. In the three-dimensional case almost the same frequencies are found, except for the horizontal boundary layers. The strong three-dimensional mixing leaves no, or only very weak, three-dimensional structures in the time-averaged nonlinear solution. Three-dimensional effects increase the maximum of the time- and depth-averaged wall-heat transfer by 15%.

1. Introduction

Natural-convection flows appear in many technical applications, like cooling of electronic systems, cooling of nuclear reactors, climate conditioning of rooms and solar collectors. The present study concentrates on the transitional flow in enclosures with differentially heated vertical walls. The horizontal walls are either conducting (they have a linear temperature profile) or adiabatic (thermally isolated). If the dimensionless temperature difference (the Rayleigh number) is sufficiently large, the flow structure is characterized by horizontal and vertical boundary layers along the walls and by a core region which is thermally stratified.

The steady two-dimensional flow of air in a square differentially heated enclosure with adiabatic horizontal walls has become a popular test case among heat-transfer computationalists. Benchmark results up to $Ra = 10^6$ were provided by de Vahl Davis & Jones (1983) and up to $Ra = 10^8$ by Le Quéré (1991). In the past few years several authors have investigated at which critical Rayleigh number the two-dimensional steady flow becomes unstable with respect to *two*-dimensional perturbations, yielding the first bifurcation of the asymptotic large-time solution. For example, Le Quéré (1987) and Le Quéré & Alziary de Roquefort (1986*a*,*b*) solved the unsteady Navier–Stokes equations for air in enclosures with adiabatic or conducting horizontal walls. The aspect ratio A_z (height over width) was varied between 1 and 10. Paolucci & Chenoweth (1989) considered air in enclosures with adiabatic horizontal walls and $0.5 \leqslant A_z \leqslant 3$. Winters (1987) detected the first bifurcation for air in a square enclosure with conducting horizontal walls by examining the eigenvalues of the two-dimensional steady flow. All these studies show that the first two-dimensional instability is due to a supercritical Hopf bifurcation, giving a transition from a steady flow to a periodic unsteady flow.

Because the enclosure flow consists of different high-Rayleigh-number structures, several more-or-less fundamental physical instability mechanisms are possible. The most unstable one (with the lowest critical Rayleigh number, Ra_{cr}) depends on the aspect ratio and on the type of boundary conditions on the horizontal walls. For adiabatic air-filled enclosures with $A_z \geqslant 4$, the first two-dimensional instability occurs in the vertical boundary layer and is of the Tollmien–Schlichting type, giving travelling waves. For adiabatic enclosures with $0.5 \leqslant A_z \leqslant 3$, the first two-dimensional instability occurs in the downstream corners of the vertical boundary layers and seems to be of the Kelvin–Helmholtz type. Conducting enclosures turn out to become unstable at a much lower critical Rayleigh number than adiabatic enclosures: a square enclosure with conducting horizontal walls has $Ra_{cr} \approx 2 \times 10^6$, whereas an adiabatic enclosure has $Ra_{cr} \approx 2 \times 10^8$. For the conducting case the first instability is related to the Rayleigh–Bénard instability, because the temperature at the horizontal walls introduces local regions with unstable stratification.

All the above mentioned computational studies are restricted to *two*-dimensional instabilities. There is no reason, however, to assume that two-dimensional perturbations are less stable than three-dimensional perturbations, as the existence of a Squire-like principle, which holds for forced-convection boundary layers, is unknown for natural-convection flows. Three-dimensional effects can be either due to the presence of lateral walls or to an intrinsic instability of the two-dimensional base flow. The former effect can be calculated by introducing three-dimensional walls with no-slip boundary conditions, whereas the latter effect can be calculated by assuming that the flow is periodic in the third direction.

The first aim of the present study is to find the influence of three-dimensional waves on the stability of two-dimensional base flows. The flow in the (x, z)-plane (where x and z are the width and height coordinates, respectively) is approximated by Chebyshev polynomials and the depth dependence is included by Fourier modes. Different depth aspect ratios will be considered, applying periodic boundary conditions in the lateral direction. Both conducting and adiabatic square enclosures ($A_z = 1$) are investigated, as several existing two-dimensional studies have also concentrated on these configurations. The range of unstable waves will be detected by solving the unsteady three-dimensional Navier–Stokes equations, in which the perturbations are linearized with respect to the two-dimensional (steady or unsteady) base flow. For

some linearly unstable wavenumbers, full nonlinear computations will also be done to investigate the structure of the supercritical three-dimensional state.

The second aim of our study is to obtain insight in the weakly turbulent two- and three-dimensional flow in a square conducting enclosure at $Ra = 10^8$. This Rayleigh number is relatively far above the critical Rayleigh number where the first unsteadiness and three-dimensional effects appear. The three-dimensional nonlinear calculation is made for a fixed depth of $0.1H$. Differences between the two- and three-dimensional flow are detected by comparison of the time-averaged solutions and by comparison of the characteristic time scales as found in the autocorrelation of the time signal at different monitoring points. The three-dimensional direct numerical simulation of the weakly turbulent flow at $Ra = 10^8$ took about 100 CPU hours on a supercomputer. In future studies the depth can be increased (say up to $2H$) and the Rayleigh number can be increased. This all requires more Chebyshev polynomials and more Fourier modes, and thus more CPU time. The calculations as presented here are intended to bring us a step closer to the direct numerical simulation of full three-dimensional turbulent natural convection in differentially heated enclosures.

2. Mathematical description

We consider a Newtonian fluid in an enclosure with height H, width W and depth D. The vertical z-axis has its positive direction opposite to that of gravity g. In the horizontal directions x is the width coordinate and y is the lateral coordinate. The left wall ($x = 0$) is hot (with uniform temperature T_h) and the right wall ($x = W$) is cold (with uniform temperature T_c). The temperature difference $\Delta T = T_h - T_c$ is assumed to be sufficiently small for the Boussinesq approximation to hold. The resulting Navier–Stokes equations read

$$\left.\begin{aligned} \frac{\partial u_i}{\partial x_i} &= 0, \\ \frac{\partial u_i}{\partial t} + \frac{\partial u_i u_j}{\partial x_j} &= -\frac{1}{\rho}\frac{\partial p}{\partial x_i} + g\beta(T - T_0)\delta_{i2} + \nu\frac{\partial^2 u_i}{\partial x_j \partial x_j}, \\ \frac{\partial T}{\partial t} + \frac{\partial u_j T}{\partial x_j} &= a\frac{\partial^2 T}{\partial x_j \partial x_j}. \end{aligned}\right\} \tag{2.1}$$

Here t is the time, $u_1 = u$, $u_2 = v$ and $u_3 = w$ are the velocity components in the $x_1 = x$, $x_2 = y$ and $x_3 = z$ directions respectively, T is the temperature, p is the pressure, ρ is the density, β is the coefficient of thermal expansion, ν is the kinematic viscosity, and a is the thermal diffusivity. These equations are made dimensionless with the length scale H, the convective time scale $t_c = H/(g\beta\Delta T H)^{1/2}$, the temperature scale $T_0 = (T_h + T_c)/2$, and the temperature difference ΔT. The convective time scale is the correct scale for the vertical boundary layers, but probably not for the core region and the horizontal boundary layers. However, in the present study the choice of the scalings is not important, as we will always specify the characteristic numbers; the dimensionless solution depends on only the Rayleigh number ($Ra = g\beta\Delta T H^3 Pr/\nu^2$), the Prandtl number ($Pr = \nu/a$), the height aspect ratio ($A_z = H/W$), and the depth aspect ratio ($A_y = D/W$). Only air ($Pr = 0.71$) in a square enclosure ($A_z = 1$) will be considered here. In what follows t^* denotes the dimensionless time ($= t/t_c$) and f^* denotes the dimensionless frequency ($= f t_c$).

The boundary conditions are: $u = v = w = 0$ at the walls $x = 0$, $x = W$, $z = 0$ and $z = H$; $T = T_h$ at $x = 0$ and $T = T_c$ at $x = W$; $\partial T/\partial y = 0$ at $z = 0$ and

$z = H$ (adiabatic case), or $T = T_h - (x/W)\Delta T$ at $z = 0$ and $z = H$ (conducting case); periodic boundary conditions at $y = 0$ and at $y = D$.

The spatial discretization for all dependent variables $\phi = \{u, v, w, p, T\}$ is based on an expansion with Chebyshev polynomials $T_n(x^*)T_m(z^*)$ in the (x, z)-plane and on an expansion with Fourier modes in the y^*-direction. Here x^*, y^* and z^* are the rescaled coordinates $x^* = 2x/W - 1$, $y^* = y/D$ and $z^* = 2z/H - 1$ respectively. The expansion reads

$$\phi(x^*, y^*, z^*, t) = \sum_{n=0}^{N} \sum_{m=0}^{M} \sum_{k=0}^{K} T_n(x^*)T_m(z^*)[a_{nmk}(t)\cos(2\pi k y^*) + b_{nmk}(t)\sin(2\pi k y^*)]; \tag{2.2}$$

$a_{nmk}(t)$ and $b_{nmk}(t)$ are the real-valued Chebyshev–Fourier coefficients, x_n^* and z_m^* are taken as the Gauss–Lobatto points, whereas the y_l^* points are distributed equidistantly.

The nonlinear terms are evaluated pseudo-spectrally. The time derivatives are discretized with second-order finite differences, applying an explicit Adams–Bashforth extrapolation to the nonlinear convection terms, and an implicit backward-Euler scheme to the diffusion terms. The pressure is evaluated fully implicitly at the new time, and is solved with the influence matrix technique as proposed by Le Quéré & Alziary de Roquefort (1982, 1985).

3. Stability

3.1. *Initial-value problem*

For a two-dimensional steady and unsteady base flow, the linear stability with respect to three-dimensional disturbances can be calculated by solving the linearized system that is found from equations (2.1) after replacing the nonlinear convective terms by their linearized counterparts,

$$u_b \frac{\partial \phi}{\partial x} + (u - u_b)\frac{\partial \phi_b}{\partial x} + w_b \frac{\partial \phi}{\partial z} + (w - w_b)\frac{\partial \phi_b}{\partial z}, \tag{3.1}$$

with $\phi = \{u, v, w, T\}$. The subscript b denotes the two-dimensional base flow, with $v_b \equiv 0$. The base flow is found by integrating the two-dimensional unsteady equations sufficiently far in time until transient effects have disappeared and the solution has reached one of the attractors of the unsteady Navier–Stokes equations.

A classical way to investigate the linear stability is the eigenvalue analysis. Disadvantages of this approach are that the base flow needs to be steady and that it cannot be used to determine the nonlinear stability. Extension of the eigenvalue method to a periodic base flow is possible, but requires the use of the more complicated Floquet theory.

Instead of solving the eigenvalue problem, in the present study the linear stability is examined by solving the linear system (2.1), using (3.1), as an initial-value problem. We introduce the perturbation $\phi'' = \phi - \phi_b$ with the form

$$\phi'' = \tilde{\phi}(x, z, t)\ \exp(i\alpha y). \tag{3.2}$$

The term $\exp(i\alpha y)$ can be rewritten as the pair $\cos(\alpha y)$ and $\sin(\alpha y)$, implying that expression (3.2) is similar to the Fourier expansion for ϕ (see (2.2)), with $K = 1$ (and $\alpha = 2\pi k/D$). This shows that the linear initial-value problem can be solved with the same code as described in §2, provided the nonlinear terms are linearized according to (3.1).

The zeroth Fourier mode is actually the two-dimensional base flow ϕ_b. As the evolution of the zeroth Fourier mode is part of the three-dimensional calculation,

the stability of both steady and unsteady (periodic or chaotic) base flows can be considered.

At $t = 0$ the two-dimensional base solution is prescribed for the zeroth Fourier mode and a small perturbation is introduced in the non-zero Fourier modes. If the energy in a given Fourier mode does not vanish, the mode is unstable. As a representative measure of the energy in the Fourier components $E_{\cos,k}(t)$ and $E_{\sin,k}(t)$ for the temperature, we take the square root of the Chebyshev–Fourier coefficients $a^2_{nmk}(t)$ and $b^2_{nmk}(t)$, respectively, averaged over the total number of Chebyshev modes. For large time, E will be solely determined by the most unstable eigenvalue $\sigma^* = \sigma + i\omega$ (with σ and ω real), implying that E increases according to $\exp(\sigma t)|\cos(\omega t)|$. It is noted that $|\cos(\omega t)|$ is periodic with the frequency ω/π, which is twice the frequency of the temperature signal itself ($f = \omega/2\pi$).

3.2. *Symmetry properties*

The two-dimensional base flow admits the skew-symmetry property $\phi_b(x,z,t) = -\phi_b(W-x, H-z, t)$, with $\phi_b = \{u, w, T - T_0\}$. Solutions ϕ'' $(= \phi - \phi_b)$ of the *linearized* three-dimensional unsteady Navier–Stokes equations admit the following two types of symmetry if the two-dimensional base flow is skew symmetric:

(i) skew symmetry with respect to $(x = W/2,\ z = H/2)$: $\phi''(x,y,z,t) = \gamma\phi''(W - x, y, H - z, t)$, with $\gamma = -1$ for $\phi = \{u, w, T\}$ and $\gamma = 1$ for $\phi = v$;

(ii) symmetry with respect to $(x = W/2,\ z = H/2)$: $\phi''(x,y,z,t) = \gamma\phi''(W - x, y, H - z, t)$, with $\gamma = 1$ for $\phi = \{u, w, T\}$ and $\gamma = -1$ for $\phi = v$.

The *nonlinear* three-dimensional equations, together with the boundary conditions specified in §2, admit three types of symmetry:

(i) plane symmetry with respect to $y = y_s$: $\phi(x,y,z,t) = \gamma\phi(x, 2y_s - y, z, t)$, with $\gamma = 1$ for $\phi = \{u, w, T - T_0\}$ and $\gamma = -1$ for $\phi = v$;

(ii) line-skew symmetry with respect to $(x = W/2, z = H/2)$: $\phi(x,y,z,t) = \gamma\phi(W - x, y, H - z, t)$, with $\gamma = -1$ for $\phi = \{u, w, T - T_0\}$ and $\gamma = 1$ for $\phi = v$;

(iii) point-skew symmetry with respect to $(x = W/2, y = y_s, z = H/2)$: $\phi(x,y,z,t) = \gamma\phi(W - x, 2y_s - y, H - z, t)$, with $\gamma = -1$ for $\phi = \{u, v, w, T - T_0\}$.

These symmetries can be broken through bifurcations. The solution will be denoted as *symmetric* or *skew symmetric* if the mirrored temperature has the same sign as or a different sign to, respectively, the original temperature. Owing to the periodic boundary conditions the solution is marginally stable in the lateral direction; i.e. if $\phi(x,y,z,t)$ is a solution of the equations, $\phi(x, y + \Delta y, z, t)$ is also a solution. Furthermore, also owing to the periodic boundary conditions, if one symmetry is found on the interval $0 \leqslant y \leqslant D$, a second symmetry of the same type also exists on the same interval. In the case that the solution is plane symmetric, $v \equiv 0$ in the planes $y = y_s$, $y = y_s + D/2$, and $y = y_s - D/2$. If the solution is plane symmetric *and* line-skew symmetric, the solution is also point-skew symmetric with respect to $(x = W/2,\ y = y_s,\ z = H/2)$.

4. Stability for an enclosure with conducting horizontal walls

4.1. *Linear stability*

The two-dimensional solution for a square enclosure with conducting horizontal walls (using 33×33 Chebyshev polynomials) is steady for $Ra = 10^6$ and for $Ra = 1.8 \times 10^6$, whereas a periodic unsteady state with $f^* = 0.255$ is found for $Ra = 2.3 \times 10^6$. Hence, $1.8 \times 10^6 < Ra_{cr,2D} < 2.3 \times 10^6$, which agrees with existing studies, like Le Quéré (1987) and Winters (1987). The isotherms for the steady two-dimensional solution at $Ra = 1.8 \times 10^6$ (see figure 1*a*) illustrate that, owing to the large Rayleigh number,

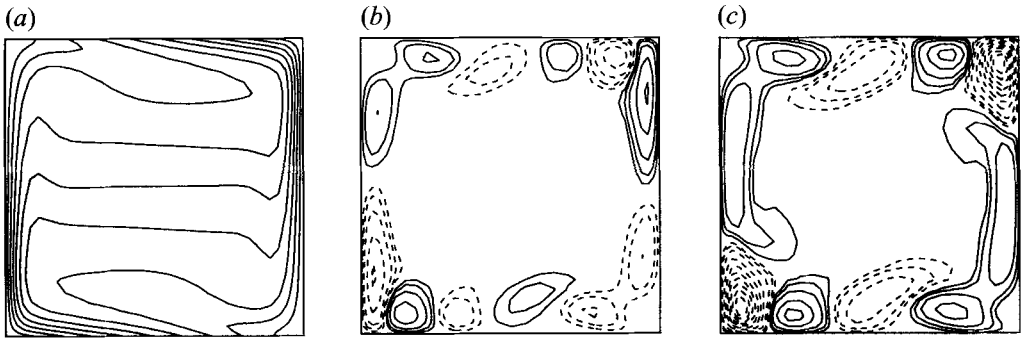

FIGURE 1. Temperature in the conducting enclosure at $Ra = 1.8 \times 10^6$: (*a*) two-dimensional base state, (*b*) unstable skew-symmetric perturbations ($\lambda = H$), (*c*) unstable symmetric perturbations ($\lambda = H$).

boundary layers have been formed along the walls with a stratified intermediate core region. The most important numerical results described in this and subsequent sections are summarized in table 1.

To determine the three-dimensional stability of these two-dimensional base states, the temperature is perturbed according to

$$(T(x,y,z) - T_0) = (T_{2D}(x,z) - T_0)(1 + \epsilon \sum_{k=0}^{K} (\cos(2\pi k y/D) + \sin(2\pi k y/D)); \quad (4.1)$$

$$0 < x < W; \quad 0 \leqslant y \leqslant D; \quad 0 < z < H,$$

with $\epsilon = 10^{-5}$. This perturbed temperature field is used as an initial solution in the three-dimensional linearized code. The two-dimensional velocity field is not explicitly perturbed, as it will be directly affected by the temperature perturbation through the buoyancy source.

At $Ra = 10^6$ all wavelengths tested were stable, whereas at $Ra = 1.8 \times 10^6$ wavelengths in the range $0.6 < \lambda/H < 1.1$ turn out to be unstable. This shows that three-dimensional perturbations are less stable than two-dimensional perturbations and that $10^6 < Ra_{cr,3D} < 1.8 \times 10^6$. The linear stability was also investigated for the two-dimensional periodic flow at $Ra = 2.3 \times 10^6$, showing that unstable waves occur in the range $0.4 < \lambda/H < 5$. The range of unstable wavelengths thus quickly extends with increasing Rayleigh number.

Some examples of the linear stability at $Ra = 1.8 \times 10^6$ are given in figure 2. The energy for $\lambda = H$ has a frequency $f^* = 0.449$ at large time. The latter frequency is not very clear in figure 2(*b*): it only thickens the line but if a portion is enlarged, the frequency shows up. We checked at different monitoring points that the temperature perturbation grows with half this frequency, i.e. $f^* = 0.224$, illustrating that the growth of a single most unstable eigenvalue is in fact observed (see §3.1).

The sudden change in the slope of the energy growth for $\lambda = H$ in figure 2(*b*) is due to the existence of two unstable eigenvalues, namely one eigenvalue (with $\sigma_1 t_c = 0.0026$, $f_1^* = 0.268$) that represents the unstable *skew-symmetric* linear perturbations, and the other eigenvalue (with $\sigma_2 t_c = 0.0118$, $f_2^* = 0.224$) that represents the unstable *symmetric* linear perturbations. As $\sigma_2 > \sigma_1$, the symmetric perturbations are even more unstable than the skew-symmetric perturbations. The eigenvalue of the skew-symmetric mode could also be found by explicitly prescribing the skew symmetry.

An animation of the perturbations in the (x,z)-plane revealed that the pertur-

		First instabilities in the conducting enclosure
2D base state	:	$1.8 \times 10^6 < Ra_{cr,2D} < 2.3 \times 10^6$ e.g. periodic state with $f^* = 0.255$ at $Ra = 2.3 \times 10^6$
3D linear stability	:	$Ra_{cr,3D} < Ra_{cr,2D}$; $10^6 < Ra_{cr,3D} < 1.8 \times 10^6$ e.g. unstable waves $0.6 < \lambda/H < 1.1$ at $Ra = 1.8 \times 10^6$, $\lambda = H$ has unstable skew-symmetric mode (with $f^* = 0.268$) and unstable symmetric mode (with $f^* = 0.224$)
3D nonlinear state	:	steady state for $Ra = 1.8 \times 10^6$ and $D = H$; periodic state with $f^* = 0.269$ if line-skew symmetry is prescribed
		First instabilities in the adiabatic enclosure
2D base state	:	$10^8 < Ra_{cr,2D} < 2 \times 10^8$ e.g. periodic state with $f^* = 0.0531$ at $Ra = 2 \times 10^8$
3D linear stability	:	$Ra_{cr,3D} < Ra_{cr,2D}$; $10^7 < Ra_{cr,3D} < 10^8$ e.g. unstable waves $0.1 < \lambda/H < 0.8$ at $Ra = 10^8$, $\lambda = H/4$ has unstable skew-symmetric mode and unstable symmetric mode (no frequency)
3D nonlinear state	:	unsteady, chaotic state for $Ra = 10^8$ and $D = H/4$, with two dominant frequencies f^* in the range 0.005–0.01 and 0.025–0.045
		Weakly turbulent flow in the conducting enclosure
2D base state	:	three dominant frequencies at $Ra = 10^8$: $f^* = 0.16$ in the horizontal boundary layer, $f^* = 0.61$ in the vertical boundary layer, $f^* = 0.077$ in the core region
3D linear stability	:	unstable waves with $\lambda/H > 0.05$ at $Ra = 10^8$
3D nonlinear state	:	three dominant frequencies for $Ra = 10^8$ with $D = H/10$: f^* in the range 0.11–0.21 in the horizontal boundary layer, $f^* = 0.59$ in the vertical boundary layer, $f^* = 0.073$ in the core region

TABLE 1. Summary of results.

bations are travelling in a clockwise direction through the horizontal and vertical boundary layers. Similar travelling perturbations were found in the supercritical two-dimensional case. Figures 1(*b*) and 1(*c*) show snapshots of the isotherms of the unstable skew-symmetric perturbations (eigenvalue σ_1, f_1), and of the unstable symmetric perturbations (eigenvalue σ_2, f_2). Solid lines denote positive temperature perturbations, and dashed lines negative. If the combination of a dark and bright spot in a clockwise direction is defined as one structure, the unstable skew-symmetric mode turns out to have five structures, whereas the symmetric mode has four structures. The skew-symmetric mode in this three-dimensional case has a close analogy with the first instability that enters the two-dimensional case: both are characterized by five structures and their frequencies are almost the same ($f^* = 0.255$ versus 0.268). In contrast to this, the four structures found for the unstable symmetric mode in the three-dimensional case were never found in any of the reported two-dimensional unsteady studies. Winters (1987), however, determined five eigenvalues of the two-dimensional steady base flow that could lead to a two-dimensional Hopf bifurcation. One of them, $f^* = 0.215$, is close to the frequency $f_2^* = 0.224$ found here for the three-dimensional instability of the symmetric mode.

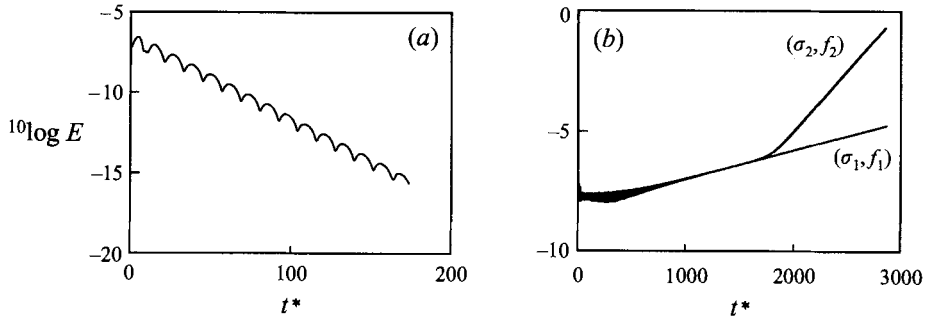

FIGURE 2. Linear stability for the conducting enclosure at $Ra = 1.8 \times 10^6$: (*a*) $E_{\cos}$ for $\lambda = H/3$, (*b*) $E_{\cos}$ for $\lambda = H$.

4.2. *Nonlinear effects*

By time integration of the three-dimensional Navier–Stokes equations (2.1), the nonlinear effects were determined for $Ra = 1.8 \times 10^6$ with four Fourier modes in the lateral direction ($K = 4$). The depth was taken as $D = H$. The nonlinear growth of the energy in the different modes closely follows the linear growth until $t^* \approx 2000$, where the nonlinear solution begins to oscillate. Later on, the oscillation suddenly stops and a steady final state is obtained. There is thus a remarkable difference between the nonlinear evolution, which gives a steady state, and the linear evolution, which gives an oscillating state. Concerning this difference, it is noted that, as explained in §3.2, the nonlinear solution *cannot* exactly admit the line-symmetric mode that was found to be most unstable in the linearized solution. The nonlinear interactions required to obtain a saturated nonlinear solution can easily lead to subsequent bifurcations, which explains the difference. On the other hand, the nonlinear solution *can* exactly admit line-skew symmetric modes. Indeed, when the line-skew symmetry was explicitly prescribed during the time integration of the nonlinear equations, an oscillating final state was found with the frequency $f^* = 0.269$, which is close to the value 0.268 found for the skew-symmetric linear mode.

4.3. *Structure of the nonlinear three-dimensional solution*

The three-dimensional steady solution at $Ra = 1.8 \times 10^6$ is both plane symmetric and point-skew symmetric. Figure 3(*a*) shows the isosurfaces of the temperature perturbations $T'' = 0.01\Delta T$ and $-0.01\Delta T$ (the perturbation T'' is defined here as the three-dimensional solution minus the depth-averaged contribution, i.e. $T'' = T - \langle T \rangle$). The solution is symmetric with respect to the planes y_s and $y_s + H/2$, and skew symmetric with respect to the points ($x = H/2$, $y = y_s + H/4$, $z = H/2$) and ($x = H/2$, $y = y_s + 3H/4$, $z = H/2$). Furthermore, the solution is also nearly skew symmetric with respect to the planes $y_s + H/4$ and $y_s + 3H/4$. As a result of this, the solution is also nearly symmetric with respect to the point ($x = H/2$, $y = y_s + H/2$, $z = H/2$) and nearly symmetric with respect to the line ($x = H/2$, $z = H/2$). Figures 3(*b*) and 3(*c*) split up the perturbation into a contribution that is exactly plane symmetric and plane-skew symmetric, and a contribution that remains, respectively. The first contribution was derived by setting the contributions of all even Fourier modes to zero. Figure 3(*c*) shows that the symmetry deviation is very small everywhere, except for the left lower and the right upper corners. It can easily be checked that these symmetries of the solution also imply that the contributions in figures 3(*b*) and 3(*c*) are symmetric and skew symmetric, respectively, with respect to the line ($x = H/2$,

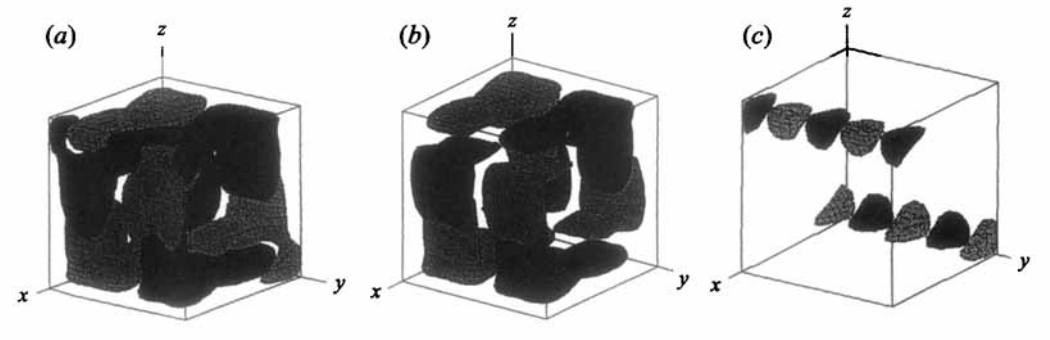

FIGURE 3. Temperature perturbation for the conducting enclosure at $Ra = 1.8 \times 10^6$ ($D = H$): (*a*) isosurfaces of $T'' = 0.01\Delta T$ and $-0.01\Delta T$, (*b*) contribution that is exactly plane and skew symmetric, (*c*) remaining contribution.

$z = H/2$). Therefore, these figures also represent the unique splitting of the solution into a line symmetric part and a skew-symmetric part.

The temperature and velocity perturbations are plotted for different planes in figure 4 (two periodic wavelengths are shown in the y-direction). The modulation of the three-dimensional waves is strongest in the horizontal and vertical boundary layers. For example, δu_{max} is 43% of $\langle u_{max} \rangle$, in which δ denotes the difference between the maximum and minimum value for a quantity in the lateral direction and u_{max} is the maximum horizontal velocity at $x = W/2$. The modulation is negligible in the core region.

There is a strong positive correlation between T'' and w'' in the boundary layers, i.e. in addition to the depth-averaged heat transfer the structures give an upward heat flux ($\langle T''w'' \rangle = \langle Tw \rangle - \langle T \rangle \langle w \rangle$ is positive). Figure 4(*a*) gives the perturbation in the plane $x = 0.038H$, which is the vertical boundary layer parallel to the hot left vertical wall. The structures in this plane can also be seen in the three-dimensional plot in figure 3(*a*). These temperature perturbations introduce a secondary recirculating flow that is parallel to the vertical wall and extends along the full enclosure height. Figure 4(*b*) gives the perturbations in the midplane $x = H/2$, which is halfway between the differentially heated vertical walls. The temperature perturbation in the horizontal boundary layers introduces convection rolls, which have a strong streamwise vorticity (longitudinal rolls). Not all the secondary fluid that reaches the vertical boundary layer is circulated within the vertical boundary layer. As shown in figures 4(*c*) and 4(*d*) (horizontal midplane $z = H/2$ and a y-plane, respectively), some fluid leaves the vertical boundary layer and travels through the core to the vertical boundary layer on the other side. This causes a recirculation in horizontal planes of the core region. Figure 4(*d*) also clearly illustrates that the solution is almost symmetric with respect to the line ($x = H/2$, $z = H/2$); the secondary flow has thus the same direction along both vertical walls.

5. Stability for an enclosure with adiabatic horizontal walls

5.1. *Linear stability*

The two-dimensional solution for the square adiabatic enclosure (using 73×73 Chebyshev polynomials) is steady for $Ra = 10^8$, whereas a periodic unsteady solution with frequency $f^* = 0.0531$ is found for $Ra = 2 \times 10^8$. These two-dimensional results agree with existing studies, like Paolucci & Chenoweth (1989). The steady

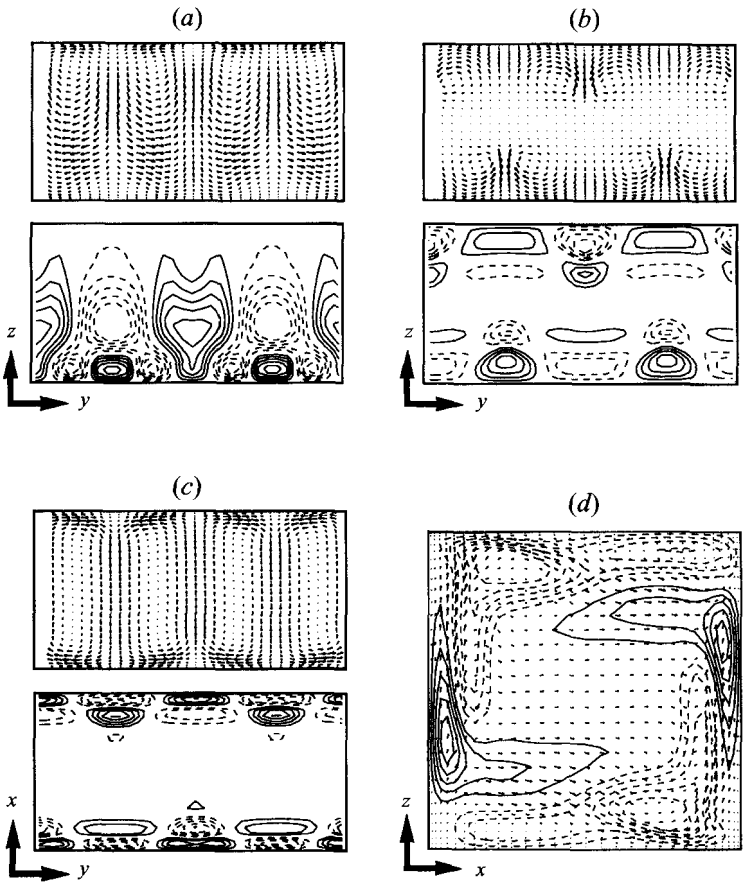

FIGURE 4. Vectors of velocity perturbations and isolines of the temperature perturbation for the conducting enclosure at $Ra = 1.8 \times 10^6$ ($D = H$): (*a*) $x = 0.038H$, (*b*) $x = H/2$, (*c*) $z = H/2$, (*d*) y-plane.

two-dimensional temperature for $Ra = 10^8$ (figure 5*a*) has thin boundary layers and a large stratified core region. The boundary layer separates and reattaches in the left upper and right lower corners.

Three-dimensional linear stability calculations with respect to these two-dimensional base states reveal that all wavelengths tested are stable for $Ra = 10^6$ and $Ra = 10^7$, whereas unstable waves occur in the range $0.1 < \lambda/H < 0.8$ for $Ra = 10^8$. Thus, it has been proven here that for an enclosure with adiabatic horizontal walls also, three-dimensional perturbations are less stable than two-dimensional perturbations.

The most unstable wavelength at $Ra = 10^8$ is $\lambda/H \approx 0.25$. Both the skew-symmetric mode and the symmetric mode for $\lambda = H/4$ are unstable, and have the same growth rate $\sigma t_c = 0.164$ for large time. No frequency is visible for large time, which indicates that the unstable eigenvalue will give a pitchfork bifurcation in the nonlinear solution. The occurrence of only one unstable eigenvalue for the adiabatic case is thus different from the conducting case, discussed in the previous section, where two distinct eigenvalues were found. The structure of unstable symmetric and skew-symmetric modes, as shown in figures 5(*b*) and 5(*c*), consists of a steady wave modulation in the core regions.

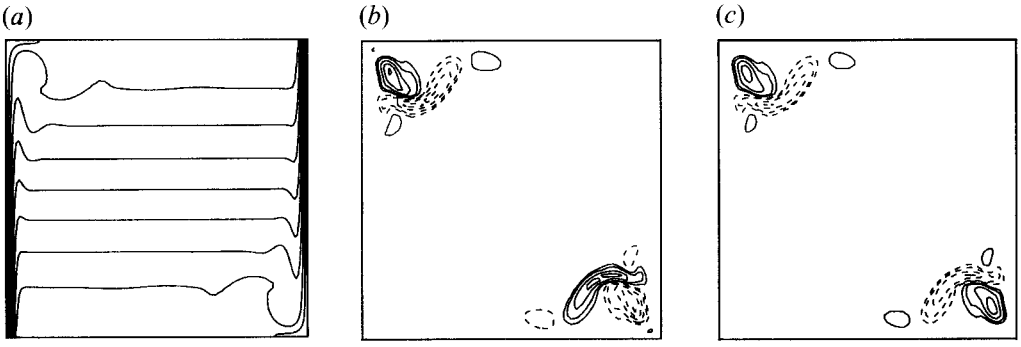

FIGURE 5. Temperature in the adiabatic enclosure at $Ra = 10^8$: (*a*) two-dimensional base state, (*b*) unstable skew-symmetric perturbations ($\lambda = H/4$), (*c*) unstable symmetric perturbations ($\lambda = H/4$).

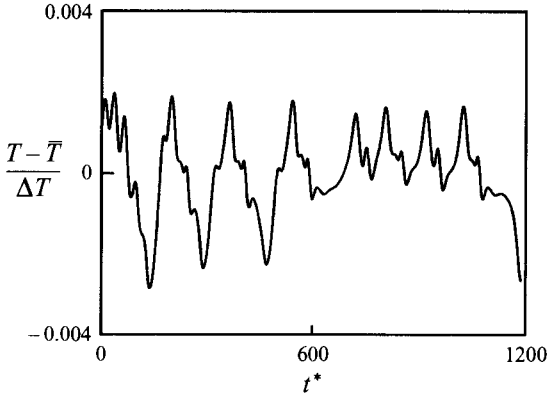

FIGURE 6. Evolution of the temperature at $x/H = 0.5$, $y/H = 0.953$ in the adiabatic enclosure with $D = H/4$ at $Ra = 10^8$.

5.2. *Nonlinear effects*

A nonlinear calculation was made for $Ra = 10^8$ with $D = H/4$, using 73×73 Chebyshev polynomials and nine points in the lateral direction ($K = 4$ Fourier modes). The two-dimensional steady base flow was perturbed with equation (4.1). Although the three-dimensional solution first seemed to converge to a new steady state, as expected from the linear stability analysis, for increasing time non-vanishing unsteadiness entered the solution. The unsteady temperature evolution for long time at $x/H = 0.5$, $y/H = 0.953$ is given in figure 6. The unsteadiness is chaotic; there are, however, two (ranges of) dominant frequencies: one very low frequency f^* in the range 0.005–0.01 and another frequency in the range 0.025–0.045. The latter frequency is close to the value 0.0531 found in the two-dimensional supercritical solution.

Averaging the unsteadiness in time gives persistent three-dimensional structures. The temperature and velocity perturbations ($\bar{\phi}'' = \bar{\phi} - \langle\bar{\phi}\rangle$, where the overbar denotes a time-averaged quantity) are shown for different planes in figure 7. Four periodic wavelengths are plotted in the lateral direction. The solution seems to be plane symmetric with respect to y_s and $y_s + D/2$, and point-skew symmetric with respect to the centre points at $y_s + D/4$ and $y_s + 3D/4$. The line-skew symmetry with respect $x = H/2$, $z = H/2$ present in the two-dimensional base flow has been broken in the three-dimensional solution. Instead, the three-dimensional solution is almost

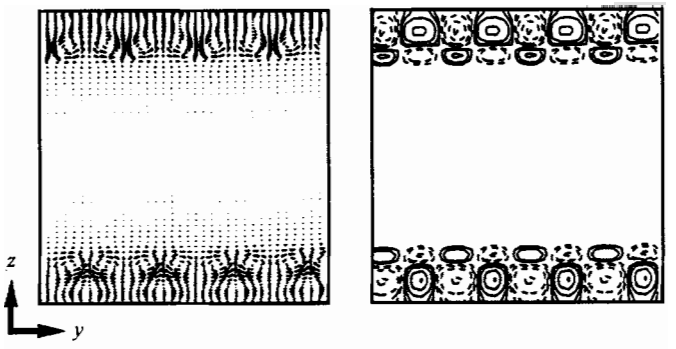

(*b*)

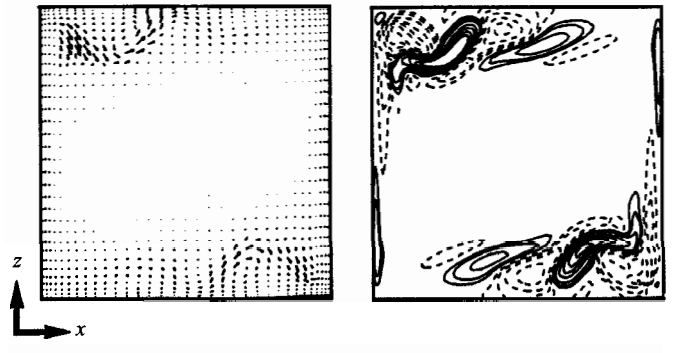

(*c*)

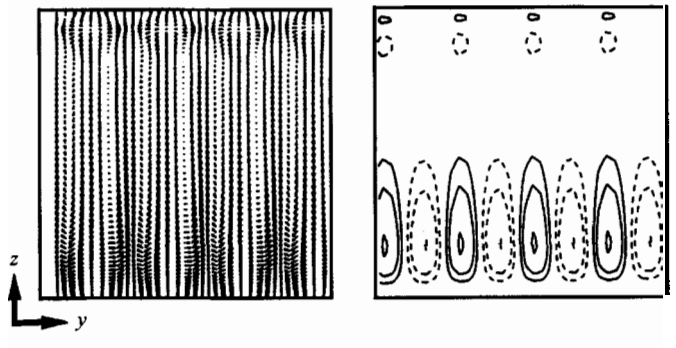

(*d*)

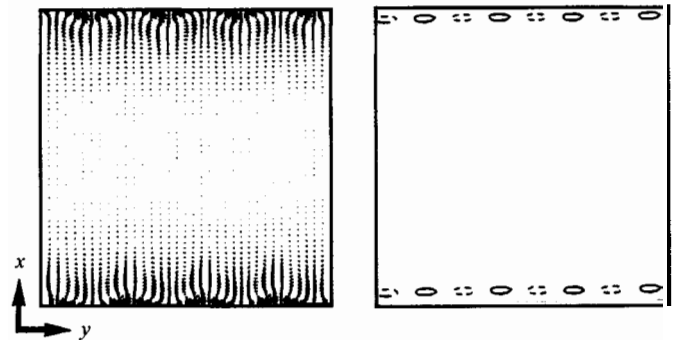

symmetric with respect to this centre line. The three-dimensional structures are strongest in the horizontal boundary layers; e.g. $\langle \overline{u} \rangle_{max}$ increases by 5% (here u_{max} is the maximum horizontal velocity at $x = H/2$).

As shown for the plane $x = H/2$ in figure 7(*a*), counter-rotating streamwise vortices are formed in the horizontal boundary layers. There is, however, a remakable difference with the longitudinal rolls that appeared along the horizontal walls for the conducting enclosure. This difference becomes clear by comparing the temperature perturbations in the y-plane (see figures 4*d*, 7*b*). The temperature perturbation in the horizontal boundary layer has a fixed sign for the conducting enclosure, whereas wave structures (with sign changes) are found for the adiabatic enclosure. As a consequence, for the first two configurations the longitudinal roll has a fixed rotation direction, independent of x, whereas the rotation direction for the latter configuration changes sign when the temperature perturbation changes sign.

For the adiabatic enclosure, figure 7(*c*) (plane $x = 0.012H$) shows the occurrence of a weak circulation parallel to the walls within the vertical boundary layers. Further, figure 7(*d*) (plane $z = H/2$) shows that there is also a weak longitudinal roll along the outer edge of the vertical boundary layers.

6. Physical origin of the instabilities

For the two-dimensional instabilities, the physical nature was indicated in earlier studies. For a conducting enclosure the first two-dimensional instability, giving a Hopf bifurcation with the frequency $f^* = 0.255$, is related to the Rayleigh–Bénard instability in an unstably stratified environment. Arguments for this were given by Le Quéré (1987) and by Janssen & Henkes (1995*a*).

With respect to the two-dimensional structure and stability for a square adiabatic enclosure, Armfield (1992) and Ravi, Henkes & Hoogendoorn (1994) have shown that the separation in the corner is due to a thermal mechanism. Le Quéré (1987) has suggested that the first instability in this enclosure was possibly due to a Kelvin–Helmholtz instability in the detached boundary layer; Janssen & Henkes (1995*b*) have performed detailed computations which strongly support the hypothesis that the frequency that first occurs, $f^* = 0.0531$, is indeed introduced by such an instability.

The nature of the three-dimensional instabilities found in the present study can be judged from the type of energy contained in the three-dimensional spatial structures. Therefore we consider the quantity $\phi(x, t)$, with $\phi' = \phi - \bar{\phi}$, and $\bar{\phi}'' = \bar{\phi} - \langle \bar{\phi} \rangle$. From the Navier–Stokes equations, using the periodicity of the solution in the lateral direction, it can be easily shown that the energy equation for $\langle \overline{u}_i'' \overline{u}_i'' \rangle$ reduces, after integration over the domain, to

$$P_{tot} + G_{tot} - \epsilon_{tot} = 0, \tag{6.1}$$

with

$$P_{tot} = \int_{x=0}^{W} \int_{z=0}^{H} P \,\mathrm{d}x\mathrm{d}z; \qquad P = \langle \overline{u_i' u_j'} \rangle \left\langle \frac{\partial \overline{u}_i''}{\partial x_j} \right\rangle - \langle \overline{u}_i'' \overline{u}_j'' \rangle \frac{\partial \langle \overline{u}_i \rangle}{\partial x_j},$$

$$G_{tot} = \int_{x=0}^{W} \int_{z=0}^{H} G \,\mathrm{d}x\mathrm{d}z; \qquad G = g\beta \langle \overline{w}'' \overline{T}'' \rangle,$$

$$\epsilon_{tot} = \int_{x=0}^{W} \int_{z=0}^{H} \epsilon \,\mathrm{d}x\mathrm{d}z; \qquad \epsilon = \nu \left\langle \frac{\partial \overline{u}_i''}{\partial x_j} \frac{\partial \overline{u}_i''}{\partial x_j} \right\rangle.$$

Here P is the energy source due to shear, G is the energy source due to buoyancy,

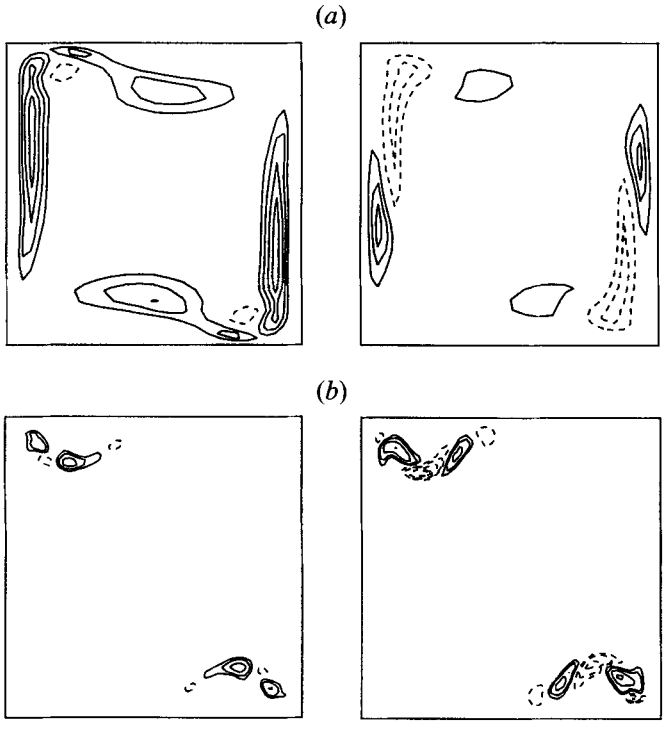

FIGURE 8. Shear source P (left-hand plots) and buoyancy source G (right-hand plots) in the energy equation for the three-dimensional structures (solid/dashed lines denote positive/negative contributions): (*a*) conducting enclosure ($D = H$, $Ra = 1.8 \times 10^6$), (*b*) adiabatic enclosure ($D = H/4$, $Ra = 10^8$).

and ϵ is the rate of energy dissipation. For a steady flow, the first term in P is zero. Evaluation of the nonlinear three-dimensional solutions reveals that the total energy source consists of 88% shear and 12% buoyancy for the conducting enclosure ($D = H$, $Ra = 1.8 \times 10^6$), and of 51% shear and 49% buoyancy for the adiabatic enclosure ($D = H/4$, $Ra = 10^8$). This indicates that the three-dimensional instabilities have a combined thermal and hydrodynamic nature.

Figure 8(*a*) shows the distribution of P and G for the conducting enclosure. The shear is largest in the horizontal and vertical boundary layers. The buoyancy is largest in part of the horizontal boundary layers, and in the upstream part of the vertical boundary layers. In the downstream part of the vertical boundary layers, the buoyancy is negative, and it thus decreases the kinetic energy in the three-dimensional structures.

Figure 8(*b*) shows the distribution of P and G for the adiabatic enclosure. Contributions are restricted to the separated horizontal boundary layers in the left upper and the right lower corners. Almost everywhere the shear is positive, but the buoyancy is alternatingly positive and negative. The positive shear may refer to a Kelvin–Helmholtz instability or to a centrifugal stability (Görtler instability). The buoyancy source and sink may be related to the temperature under- and overshoots that caused the separation of the horizontal boundary layers.

Janssen & Henkes (1995*a*) and Janssen (1994) have performed computations with a finite-volume method for three-dimensional rectangular enclosures. In contrast to the periodic boundary conditions as applied in the present calculations, they considered fixed, adiabatic lateral walls in the lateral direction. Symmetry with respect to the

midplane $y = D/2$, and with respect to the line $x = W/2$, $z = H/2$ was explicitly prescribed. For the square enclosure with conducting horizontal walls, a spatial wave modulation was found at $Ra = 2.5 \times 10^6$, with $\lambda \approx 0.68H$ for $A_y = 1$ and $\lambda \approx 0.9H$ for $A_y = 2$. These wavelengths are within the range $0.6 < \lambda < 1.1$, which we found to be linearly unstable in §4.1. The occurrence of the wave modulation shows that the lateral walls only affect the solution close to the wall and that the instability is due to an intrinsic three-dimensional instability of the two-dimensional base solution. Janssen & Henkes find a periodic supercritical flow (with frequency $f^* = 0.266$), whereas we find a steady state. This difference is most probably due to the prescribed symmetry, as we also found an oscillating state with about the same frequency if symmetry was prescribed (§§4.1 and 4.2). In a cubical enclosure at $Ra = 10^8$, with adiabatic horizontal walls and fixed lateral walls, Janssen (1994) finds a steady three-dimensional state, whereas we find an unsteady three-dimensional state (using periodic boundary conditions). This difference is most probably due to the difference in lateral boundary conditions, as Janssen also finds an oscillating state if A_y is increased from 1 to 2. His solution shows a wave modulation with wavelength $\lambda \approx 0.18H$, which is close to the wavelength $\lambda = H/4$, that we calculated to be the most unstable linear wave. Our time-averaged three-dimensional solution for $D = H/4$ is very close to Janssen's three-dimensional steady solution not too close to the lateral walls. For example $\delta T_{max} = 0.034\Delta T$ in the cubical enclosure, and $0.030\Delta T$ in the enclosure with $D = H/4$ and periodic boundary conditions.

To the authors' knowledge, up to now no experimental studies on the intrinsic three-dimensional instability of natural-convection flow in square differentially heated enclosures exist. Briggs & Jones (1985) have performed measurements in an almost cubical, differentially heated enclosure filled with air. The horizontal walls were conducting, and the lateral walls were adiabatic. They measured the different frequencies, which were also found in subsequent two-dimensional numerical studies, but they do not report any three-dimensional structures. Hiller *et al.* (1989) have measured the high-Prandtl-number flow in a cubical differentially heated enclosure, with adiabatic horizontal walls and adiabatic lateral walls. When the Rayleigh number is increased they find a continuous change in the topological structure of the flow, which includes three-dimensional vortical behaviour. Hiller *et al.* suggest that these effects are due to their failure to achieve true adiabatic conditions on the lateral walls. We agree with this, and think that their three-dimensional structures are not due to the intrinsic three-dimensional instability of the two-dimensional base flow investigated in the present theoretical study.

There is thus a need for new experiments that can validate our results. A suitable test configuration is the differentially heated square enclosure with conducting horizontal walls (which are much easier to realize than adiabatic horizontal walls). The lateral walls should be sufficiently isolated to minimize their effect on the stability. The depth of the enclosure should be sufficiently large (say $A_y \geqslant 3$) for the most unstable waves ($\lambda \approx H$) to fit several times in the enclosure, and for the lateral walls to have a negligible effect on the three-dimensional stability.

7. Weakly turbulent flow for the square conducting enclosure

7.1. *Two-dimensional approach*

As described in §3.1, the first instability for the two-dimensional square enclosure with conducting horizontal walls occurs at $1.8 \times 10^6 < Ra_{cr,2D} < 2.3 \times 10^6$, giving a Hopf bifurcation with $f^* = 0.255$. We have further increased the Rayleigh number

	61×61	81×81		
t^*_{av}	475	475	950	1900
$\frac{\overline{w}_{max}}{(g\beta\Delta TH)^{1/2}}$	0.288	0.287	0.287	0.287
$\frac{\overline{u}_{max}}{(g\beta\Delta TH)^{1/2}}$	0.137	0.136	0.134	0.137
$\overline{Nu}_w$	23.8	23.8	23.9	23.9
$\overline{S}$	0.367	0.388	0.391	0.389
$\frac{k_{max}}{g\beta\Delta TH}$	0.00202	0.00192	0.00185	0.00180
$\frac{\overline{u'w'}_{max}}{g\beta\Delta TH}$	0.000142	0.000140	0.000133	0.000132
$\frac{\overline{T'^2}_{max}}{\Delta T^2}$	0.00424	0.00369	0.00384	0.00384

TABLE 2. Some characteristic time-averaged values for the two-dimensional conducting enclosure at $Ra = 10^8$.

up to 10^8. This Rayleigh number is so high that the unsteady solution at large time can be referred to as chaotic, highly transitional, or weakly turbulent. To examine the unsteady flow evolution, different monitoring points for the temperature were considered, which are positioned in the horizontal boundary layer, in the vertical boundary layer, and in the core region.

We are interested in the large-time state of the solution, and not in the decaying transients caused by the specific initial solution. As the asymptotic state at $Ra = 10^8$ is unsteady and non-periodic, it is difficult to detect when the transients have decayed. In earlier two-dimensional studies, in which either a steady, or periodic or quasi-periodic asymptotic state was found, the transients took about one tenth of the diffusion time scale H^2/ν, which is the time needed to damp the internal wave activity in the core region. For example, Schladow, Patterson & Street (1989) made a detailed numerical analysis of the transients to a steady final state for water in a two-dimensional square differentially heated enclosure filled with water. Using these findings, for the present case the decay time is guessed to be about $t^* \approx 1200$. As a consequence, the unsteady solution with an 81×81 resolution was first integrated for more than 1000 convective time scales, before the time averaging was started.

The averaged solution over the time $t^*_{av} = 475$, and over the double averaging times 950 and 1900, are compared for different characteristic quantities in table 2. The table gives the maximum for $\overline{w}$, k, $\overline{T'^2}$ and $\overline{u'w'}$ at half the enclosure height; the maximum of $\overline{u}$ at half the enclosure width; the temperature stratification $\overline{S}$ at the enclosure centre (with $S = (H/\Delta T)\left(\partial T/\partial y\right)_c$); and the time- and height-averaged heat transfer through the hot wall, $\overline{Nu}_w$ (where Nu_w is the height averaged value of $(H/\Delta T)\left(\partial T/\partial x\right)_w$). The turbulent kinetic energy is defined as $k = (\overline{u'^2} + \overline{w'^2})/2$. The table shows that both the first-order statistics ($\overline{w}_{max}$, $\overline{u}_{max}$, $\overline{Nu}_w$ and $\overline{S}$) and the second-order statistics (k_{max}, $\overline{u'w'}_{max}$, $\overline{T'^2}$), for the 81×81 resolution and with $t^*_{av} = 1900$, have become practically independent of the averaging time. When the time integration was stopped, the first-order and second-order statistics had become almost fully symmetric with respect to the enclosure centre (differences are below

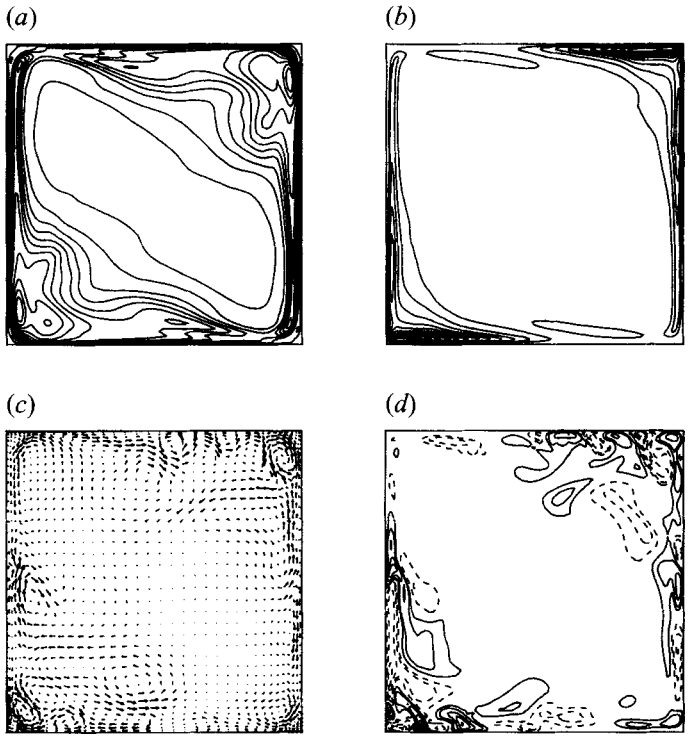

FIGURE 9. Conducting enclosure at $Ra = 10^8$: (*a*) isolines of turbulent kinetic energy, (b) isolines of temperature variance, (*c*) instantaneous velocity fluctuations, (*d*) instantaneous temperature fluctuations.

3%). To verify the spatial accuracy, the table also includes the solution for the 61×61 resolution, which is averaged over the time $t^*_{av} = 475$.

7.2. *Two-dimensional structures*

As was also found for $Ra = 10^6$, the core at $Ra = 10^8$ is still well stratified and almost motionless. The largest velocities and the largest temperature gradients occur in the horizontal and vertical boundary layers. The perturbation, as represented by k (figure 9*a*) and $\overline{T'^2}$ (figure 9*b*), are concentrated in part of the horizontal and vertical boundary layers.

Typical instantaneous fields for the velocity and temperature perturbations are shown in figures 9(*c*) and 9(*d*). Fluctuating structures along the horizontal walls are either convected within the horizontal mean flow or directly dispatched from the horizontal boundary layers into the core region like thermal plumes. Perturbations coming from the horizontal boundary layers are also convected into the vertical boundary layers where they propagate as travelling waves.

The left-hand graphs in figure 10 show typical time signals of the temperature at different monitoring points, and the right-hand graphs give the corresponding autocorrelation functions. The difference between the curves for an averaging time $t^*_{av} = 778$ and twice this time is only small, which confirms the accuracy. The best-correlated time scale t_b (or frequency $f = 1/t_b$) is represented by the first local maximum in the auto correlation function.

The monitoring point in the horizontal boundary layer has the dominant frequency $f^* = 0.16$. This is somewhat below the first frequency $f^* = 0.255$, which entered the

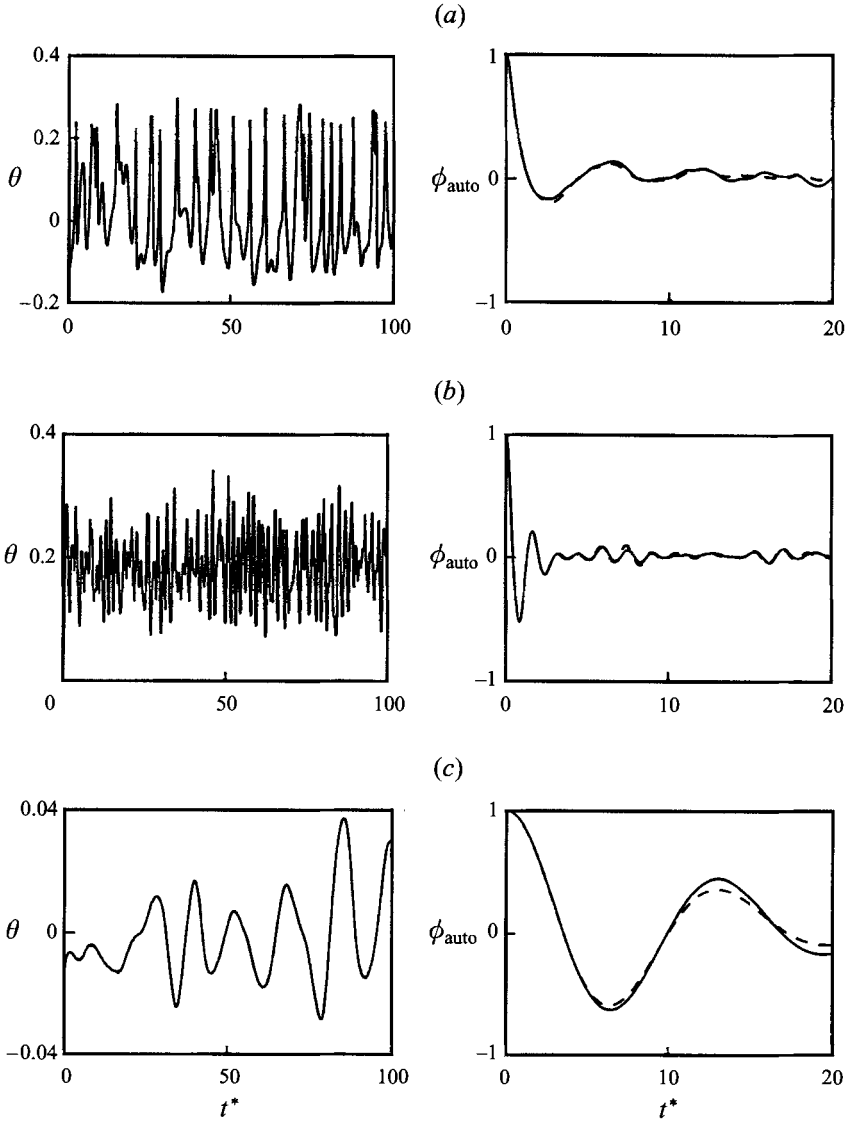

FIGURE 10. Analysis of the temperature fluctuations at different monitoring points in the conducting enclosure at $Ra = 10^8$; left-hand graphs give part of the time signal, and right-hand graphs give the autocorrelation (—, $t^*_{av} = 1556$; - -, $t^*_{av} = 778$): (*a*) $x/H = 0.054$, $z/H = 0.018$, (*b*) $x/H = 0.018$, $z/H = 0.75$, (*c*) $x/H = 0.5$, $z/H = 0.5$; $\theta = (T - T_0)/\Delta T$.

solution at $Ra_{cr} \approx 2 \times 10^6$. The monitoring point in the vertical boundary layer at $y/H = 0.75$ shows a clear dominant frequency $f^* = 0.61$, close to the boundary-layer frequency $f^* = 0.61$ found by Paolucci & Chenoweth (1989) for an *adiabatic* square enclosure at $Ra = 3 \times 10^8$. The enclosure centre shows a dominant frequency $f^* = 0.077$.

The dominant frequencies found in the different regions of the enclosure seem to be related to the following physical mechanisms. The first instability in the two-dimensional conducting enclosure (at $Ra_{cr} \approx 2 \times 10^6$, with $f^* = 0.255$) is known to be due to a Rayleigh–Bénard-like instability in the locally unstable vertical temperature gradient in the horizontal boundary layers. The same mechanism still seems to be present at $Ra = 10^8$, giving the dominant frequency $f^* = 0.16$ (most clearly visible

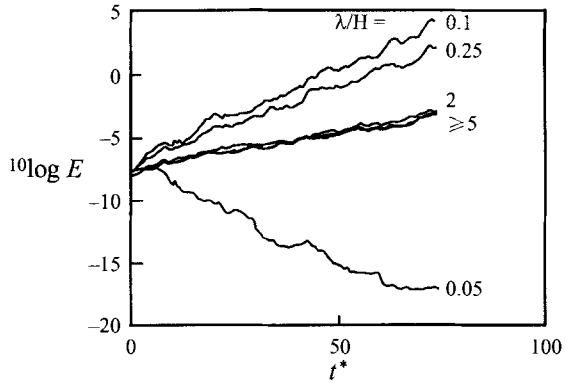

FIGURE 11. Linear stability for different wavelengths in the conducting enclosure at $Ra = 10^8$.

in the horizontal boundary layers and in the initial part of the vertical boundary layers). These Rayleigh–Bénard oscillations seem to trigger Tollmien–Schlichting-like travelling waves at heights $z > H/2$ in the vertical boundary layer along the hot wall, with the frequency $f^* = 0.61$.

The low frequency $f^* = 0.077$ in the core seems to be related to internal wave motion, which probably gains its energy from the Rayleigh–Bénard instability along the horizontal walls. As shown by Turner (1973) internal waves with frequency f propagate at an angle θ with the horizontal, where θ is given by

$$\cos\theta = \frac{2\pi}{S^{1/2}} f^*. \tag{7.1}$$

Here S is the gradient of the thermal stratification, $H/\Delta T\,(\partial T/\partial y)$. As S turns out to be almost constant in most of the core region of the heated enclosure, we can expect that equation (7.1) provides a good approximation. Because $|\cos\theta| \leqslant 1$, the maximum allowable core frequency is $f_{BV}{}^* = S^{1/2}/2\pi$; here f_{BV} is the so-called Brunt–Väisälä frequency. For the present case $\overline{S} = 0.39$, giving $f_{BV}{}^* = 0.099$. Indeed the dominant frequency is below, but close to, f_{BV}. If the analogy with (7.1) strictly holds, the dominant frequency corresponds to internal waves with $\theta = 39°$. According to equation (7.1) the core can only absorb energy in the frequency range below $f_{BV}{}^* = 0.099$. Therefore the core cannot oscillate with the same frequency as the horizontal boundary layers, i.e. with $f^* = 0.16$. Physically, the plumes that are dispatched from the horizontal boundary layers transfer energy to the core region.

7.3. *Three-dimensional approach*

First a linear three-dimensional stability analysis was performed for the two-dimensional unsteady base flow. The linearized equations were solved, as described in §3.1, in which the two-dimensional unsteady base flow appears as the zeroth Fourier mode. The perturbation energy in wavelengths $0.05H$ and lower damps to machine accuracy, whereas the energy in wavelengths $0.1H$ and larger are growing (see figure 11). Among the wavelengths tested, $\lambda = 0.1H$ is most unstable, having a growth rate $\sigma t_c = 0.33$. It is noted that increasing the wavelength to very large values does not lead to stability ($\sigma t_c = 0.13$ for $\lambda \to \infty$), because of the chaotic state of the two-dimensional base flow.

In order to prevent the three-dimensional nonlinear calculation from blowing up, linearly stable Fourier modes must be included in the lateral direction. In this way

	2D 81 × 81	3D 109 × 109 × 9		
t^*_{av}	1900	100	220	400
$\frac{\langle\overline{w}\rangle_{max}}{(g\beta\Delta TH)^{1/2}}$	0.287	0.280	0.281	0.283
$\frac{\langle\overline{u}\rangle_{max}}{(g\beta\Delta TH)^{1/2}}$	0.137	0.163	0.165	0.166
$\langle\overline{Nu}\rangle_w$	23.7	24.7	24.7	24.8
$\langle\overline{S}\rangle$	0.389	0.349	0.348	0.343
$\frac{\langle k\rangle_{max}}{g\beta\Delta TH}$	0.00180	0.00219	0.00222	0.00223
$\frac{\langle\overline{u'w'}\rangle_{max}}{g\beta\Delta TH}$	0.000132	0.000322	0.000341	0.000317
$\frac{\langle\overline{T'^2}\rangle_{max}}{\Delta T^2}$	0.00384	0.00316	0.00327	0.00320

TABLE 3. Some characteristic time- and depth-averaged values for the two-dimensional and three-dimensional conducting enclosure at $Ra = 10^8$ ($D = 0.1H$).

energy from linearly unstable modes can be nonlinearly transferred to other modes and can be dissipated by the linearly stable modes. A nonlinear three-dimensional calculation was performed for $D = 0.1H$ with four Fourier modes, corresponding to wavelengths $0.1H$, $0.05H$, $0.033H$ and $0.025H$; thus there are nine physical grid points in the y-direction. This calculation does indeed contain dissipating modes. The two-dimensional solution at large time, described in the previous section, together with the initial perturbation (4.1) was used to start the three-dimensional calculation. The time integration for the 109 × 109 resolution was carried out over 340 convective time scales, before the time averaging was started.

7.4. *Three-dimensional structures*

Some characteristic time- and depth-averaged quantities are summarized in table 3 and compared with the two-dimensional solution. For the three-dimensional solution, the table also compares the results for the averaging times $t^*_{av} = 100$, 220 and 400, confirming that the first- and second-order statistics have become almost independent of the averaging time. In the table, the three-dimensional turbulent kinetic energy is defined as $k = (\overline{u'^2} + \overline{v'^2} + \overline{w'^2})/2$. The accuracy of the second-order statistics is also confirmed by the good symmetry that is obtained between the quantities along the hot and cold wall. For example figure 12 shows the maximum of $\langle k\rangle$ and $\langle\overline{T'^2}\rangle$ as a function of the height along the hot and cold walls (the maximum is taken over $0 \leqslant x \leqslant H/2$ and $H/2 \leqslant x \leqslant H$ respectively). To check the symmetry, the z-coordinate along the cold wall is plotted reversed, i.e. $z = 0$ at the ceiling and $z = H$ at the floor. The solid/dashed lines denote the maximum along the hot/cold wall, respectively. For $\langle k\rangle_{max}$ along the hot wall (figure 12*a*), three-dimensional effects give a decrease of the kinetic energy below $z = H/5$ and an increase further downstream. For $\langle\overline{T'^2}\rangle_{max}$ along the hot wall (figure 12*b*) the effect is exactly opposite: three-dimensional effects increase the temperature variance below $z = H/5$ and give a slight decrease further downstream.

Different time- and depth-averaged three-dimensional quantities are compared with

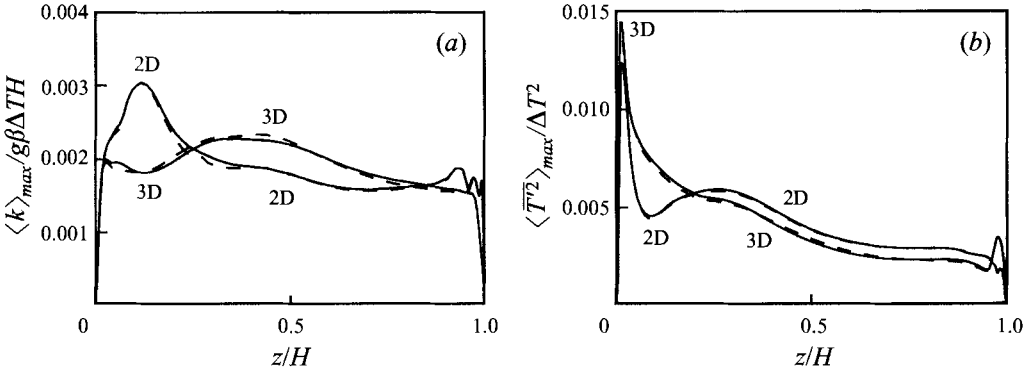

FIGURE 12. Two- and three-dimensional averaged quantities along the hot (—) and cold (- -) walls of the conducting enclosure at $Ra = 10^8$ with $D = 0.1H$: (*a*) $\langle k \rangle_{max}$, (*b*) $\langle \overline{T'^2} \rangle_{max}$.

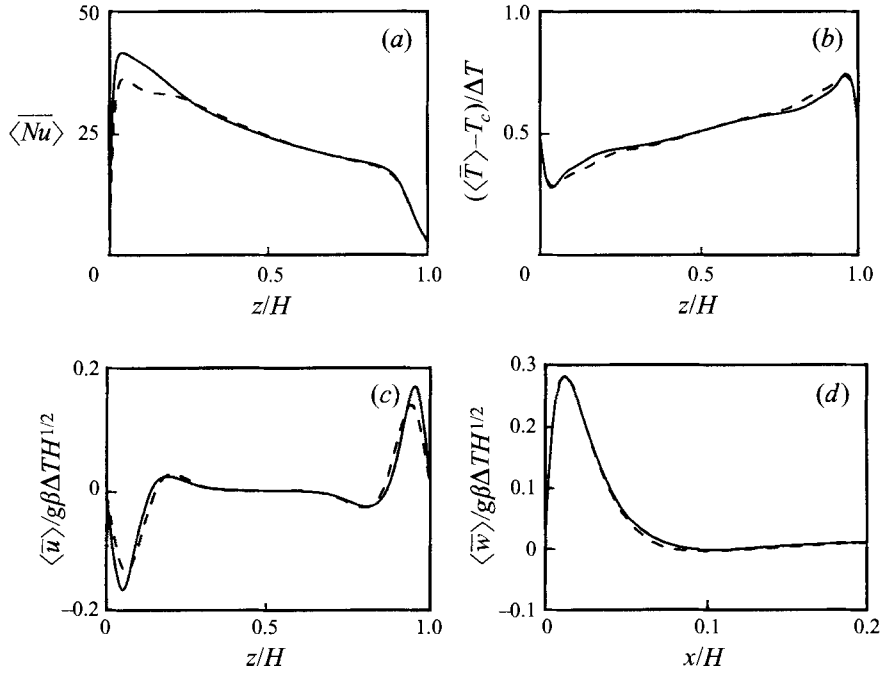

FIGURE 13. Two- and three-dimensional averaged quantities for the conducting enclosure at $Ra = 10^8$, with $D = 0.1H$ in the three-dimensional case (—, three-dimensional; - -, two-dimensional): (*a*) Nusselt number along the hot wall, $\langle \overline{Nu} \rangle_w$, (*b*) core stratification, $\langle \overline{T} \rangle$ at $x = H/2$, (*c*) horizontal velocity at $x = H/2$, (*d*) vertical velocity at $z = H/2$.

the time-averaged two-dimensional values in figure 13. The three-dimensional effects increase $\langle \overline{Nu} \rangle_{max}$ by 15% (figure 13*a*) and decrease $\langle \overline{S} \rangle$ by 12% (figure 13*b*). The three-dimensional effect on the time- and depth-averaged horizontal velocity at half the enclosure width (figure 13*c*) is large: $\langle \overline{u} \rangle_{max}$ increases by 21%. Only a small three-dimensional effect is found for the vertical velocity profile at half the enclosure height (figure 13*d*): $\langle \overline{w} \rangle_{max}$ decreases by 2%. Different turbulence quantities were also compared, like $\langle k \rangle$, $\langle \overline{u'w'} \rangle$, $\langle \epsilon \rangle$, $\langle \overline{T'^2} \rangle$, and the turbulent viscosity ν_t, modelled as $\nu_t = c_\mu k^2/\epsilon$, with $c_\mu = 0.09$. Some of these quantities in the vertical boundary layer in

the three-dimensional case indicate an increase of turbulence, whereas others indicate a decrease. For example, although the turbulent kinetic energy is increased, the turbulent energy dissipation rate increases as well, giving a decrease of the turbulent viscosity; in the vertical boundary layer at $z = H/2$ the maximum turbulent viscosity ν_t/ν is 7.3 in the two-dimensional case and 2.4 in the three-dimensional case.

In contrast to the time- and depth-averaged values themselves, differences between the time-averaged values at the same x,z position, but at a different y-position, still have not become sufficiently independent of time. However, at the time at which the calculation was stopped, the three-dimensional modulation was already below 1%. This shows that the unsteady processes strongly mix the three-dimensional structures, leaving no, or only very weak, persistent time-averaged three-dimensional structures.

Comparison of the autocorrelations, as determined for $t^*_{av} = 400$ and 220, shows that there still is a slight dependence on the averaging time, but that the dominant frequencies have already become almost fully independent of the averaging time. The dominant frequencies at two monitoring points in the horizontal boundary layer are $f^* = 0.11$ and 0.21, whereas both points have the dominant frequency $f^* = 0.16$ in the two-dimensional case. The vertical boundary layer at $y/H = 0.75$ shows the dominant frequency $f^* = 0.59$, which is almost the same as in the two-dimensional case ($f^* = 0.61$). The enclosure centre shows a dominant frequency $f^* = 0.073$, which is only slightly smaller than in the two-dimensional case ($f^* = 0.077$). It can thus be concluded that the largest three-dimensional effects on the dominant frequencies are found in the horizontal boundary layer.

8. Conclusions

It has been shown that three-dimensional perturbations initiate the transition of natural-convection flow of air in differentially heated square enclosures. Therefore the assumption of two-dimensionality, as made in earlier stability studies, is not correct. The two most unstable modes, found in the linear stability analysis for the conducting enclosure, have a lateral wavelength of approximately the enclosure size, and they are characterized by four and five travelling structures, respectively, within the boundary layers. The most unstable modes for the adiabatic enclosure give a steady modulation in the separated boundary layers in the corner regions. The nonlinear solution at slightly supercritical Rayleigh numbers is already different from what is expected from the linear stability, and is of a steady nature in the conducting case and has two distinct dominant frequencies in the adiabatic enclosure, one of which is close to the value found in existing two-dimensional studies. For both cases the three-dimensional nonlinear solution is characterized by strong counter-rotating convection rolls along the horizontal wall. Analysis of the energy budgets has shown that these rolls are of a combined thermal and hydrodynamic nature.

In addition to the stability analyses, two- and three-dimensional weakly turbulent flows were also accurately computed in a conducting enclosure, at a Rayleigh number which is two orders of magnitude larger than the value at which the first instabilities occur. The unsteady, three-dimensional mixing is so strong that no, or only weak, persistent structures remain in the time-averaged solution. The most significant three-dimensional effect, as compared to the two-dimensional case, is the increase of the the maximum in the time- and depth-averaged wall heat transfer by 15%. The three-dimensional effect on the dominant frequencies is strongest in the horizontal boundary layers, and only very small in the other regions. Some of the dominant frequencies in both the two- and three-dimensional weakly turbulent flow are close to the values

found in two-dimensional stability analyses in the conducting and adiabatic enclosures, which shows that the fundamental two-dimensional instabilities, like the Rayleigh–Bénard instability and the Tollmien–Schlichting instability, keep their identity.

This work was supported by the Royal Netherlands Academy for Arts and Sciences (KNAW). Most of the computations were run on the CRAY of IDRIS. The research was performed when the first author (R.A.W.M.H.) was on leave at the institute of the second author (P.Q.).

REFERENCES

ARMFIELD, S. 1992 Conduction blocking effects in stratified intrusion jets. *Proc. 11th Australasian Fluid Mech. Conf.*, pp. 335–339.

BRIGGS, D. G. & JONES, D. N. 1985 Two-dimensional periodic natural convection in a rectangular enclosure of aspect ratio one. *Trans. ASME J. Heat Transfer* **107**, 850–854.

HILLER, W. J., KOCH, S., KOWALEWSKI, T. A., VAHL DAVIS, G. DE & BEHNIA, M. 1989 Experimental and numerical investigation of natural convection in a cube with two heated side walls. In *Topological Fluid Mechanics* (ed. H. K. Moffatt & A. Tsinober), pp. 717–726. Cambridge University Press.

JANSSEN, R. J. A. 1994 Instabilities in natural-convection flows in cavities. PhD thesis, Delft University of Technology, The Netherlands.

JANSSEN, R. J. A. & HENKES, R. A. W. M. 1995*a* The first instability mechanism in differentially heated cavities with conducting horizontal walls. *Trans. ASME J. Heat Transfer* **117**, 626–633.

JANSSEN, R. J. A. & HENKES, R. A. W. M. 1995*b* Influence of Prandtl number on instability mechanisms and transition in a differentially heated square cavity. *J. Fluid Mech.* **290**, 319–344.

JANSSEN, R. J. A., HENKES, R. A. W. M. & HOOGENDOORN, C. J. 1993 Transition to time periodicity of a natural-convection flow in a three-dimensional differentially heated cavity. *Intl J. Heat Mass Transfer* **36**, 2927–2940.

LE QUÉRÉ, P. 1987 Etude de la transition à l'instationnarité des écoulements de convection naturelle en cavité verticale différentiellement chauffée par méthodes spectrales Chebyshev. PhD thesis, University of Poitiers.

LE QUÉRÉ, P. 1991 Accurate solutions to the square thermally driven cavity at high Rayleigh number. *Computers Fluids* **20**, 29–41.

LE QUÉRÉ, P. & ALZIARY DE ROQUEFORT, T. 1982 Sur une méthode spectrale semi-implicit pour la résolution des équations de Navier-Stokes d'un écoulement bidimensionnel visqueux incompressible. *C.R. Acad. Sci. Paris* **294** II, 941–944.

LE QUÉRÉ, P. & ALZIARY DE ROQUEFORT, T. 1985 Computation of natural convection in two-dimensional cavities with Chebyshev polynomials. *J. Comput. Phys.* **57**, 210–228.

LE QUÉRÉ, P. & ALZIARY DE ROQUEFORT, T. 1986*a* Transition to unsteady natural convection of air in differentially heated vertical cavities. *ASME Heat Transfer Div.* Vol. 60, pp. 29–39.

LE QUÉRÉ, P. & ALZIARY DE ROQUEFORT, T. 1986*b* Transition to unsteady natural convection of air in vertical differentially heated cavities: influence of thermal boundary conditions on the horizontal walls. *Proc. 8th Intl Heat Transfer Conf., San Francisco*, pp. 1533–1538.

PAOLUCCI, S. & CHENOWETH, D. R. 1989 Transition to chaos in a differentially heated vertical cavity. *J. Fluid Mech.* **201**, 379–410.

RAVI, M. R., HENKES, R. A. W. M. & HOOGENDOORN, C. J. 1994 On the high Rayleigh number structure of steady laminar natural-convection flow in a square enclosure. *J. Fluid Mech.* **262**, 325–351.

SCHLADOW, S.G., PATTERSON, J.C. & STREET, R.L. 1989 Transient flow in a side-heated cavity at high Rayleigh number: a numerical study. *J. Fluid Mech.* **200**, 121–148.

TURNER, J.S. 1973 *Buoyancy Effects in Fluids.* Cambridge University Press.

VAHL DAVIS, G. DE & JONES, I. P. 1983 Natural convection in a square cavity: a comparison exercise. *Intl J. Num. Meth. Fluids* **3**, 227–248.

WINTERS, K. H. 1987 Hopf bifurcation in the double-glazing problem with conducting boundaries. *J. Heat Transfer* **109**, 894–898.